Materials Science in Semiconductor Processing 183 (2024) 108733

Contents lists available at ScienceDirect

Materials Science in Semiconductor Processing

journal homepage: www.elsevier.com/locate/mssp

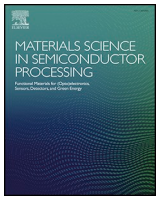

Fabrication of ZnO–Al_2O_3 inverse opals with atomic layer deposited Amorphous-Al_2O_3 for enhanced photocatalysis

Hamsasew Hankebo Lemago [a,f,**], Nour Khauli [a], Dóra Hessz [c,d], Tamás Igricz [e], Pál Petra [b], Csaba Cserháti [b], Baradács Eszter Mónika [b], Bence Parditka [b], Zoltán Erdélyi [b], Imre Miklós Szilágyi [a,*]

[a] Department of Inorganic and Analytical Chemistry, Faculty of Chemical Technology and Biotechnology, Budapest University of Technology and Economics, Műegyetem rkp. 3, H-1111, Budapest, Hungary
[b] Department of Solid-State Physics, Faculty of Sciences and Technology, University of Debrecen, P.O. Box 400, 4002, Debrecen, Hungary
[c] Department of Physical Chemistry and Materials Science, Faculty of Chemical and Bioengineering, Budapest University of Technology and Economics, Műegyetem rkp. 3, H-1111, Budapest, Hungary
[d] MTA-BME Lendület Quantum Chemistry Research Group, Műegyetem rkp. 3., H-1111, Budapest, Hungary
[e] Department of Organic Chemistry and Technology, Faculty of Chemical Technology and Biotechnology, Budapest University of Technology and Economics, H-1111 Budapest, Hungary
[f] Department of Chemistry, College of Natural and Computational Science, Wachemo University, Hossana, 667, Ethiopia

ARTICLE INFO

Keywords:
ZnO inverse opal
ZnO–Al_2O_3 TALD composite
ZnO–Al_2O_3 PEALD composite
Photocatalysis

ABSTRACT

Zinc oxide inverse opal (IO) has excellent photocatalytic properties, while Al_2O_3 has high chemical stability and negligible photocatalytic activity. However, combining these materials creates a crystalline ZnO-amorphous Al_2O_3 composite IO photonic crystal material with improved photocatalytic performance. In this study, ZnO IO and ZnO–Al_2O_3 combined structures were grown on self-assembled polystyrene (PS) nanosphere templates. ZnO layer was coated by thermal atomic layer deposition (TALD) in the pores of the template, and the template was then removed by annealing to yield a self-standing ZnO IO nanostructure. An ultra-thin film of Al_2O_3 was coated on the top of ZnO IO by TALD or plasma-enhanced ALD (PEALD). SEM imaging, Raman spectroscopy, and XRD analysis confirmed the presence of a periodically arranged, and wurtzite ZnO IO structure, with an amorphous Al_2O_3 layer on top. The UV–Vis results demonstrated distinctive absorption bands in both regions, with a notable increase in visible light absorption attributed to the slow photon effect within the near-bandgap region of the photonic materials. The ZnO/Al_2O_3-TALD photocatalyst exhibited enhanced photocatalytic performance in degrading various pollutants including methylene blue, rhodamine 6G, and 4-nitrophenol under visible light illumination compared to its pristine IO and PEALD composite counterparts. This is attributed to its periodic arrangement of the IO structure that acts as a photonic crystal, precisely controlling light interaction through photonic band gap manipulation and the slow photon effect. This tailored light manipulation within the visible spectrum significantly enhances photodegradation efficiency.

1. Introduction

Over the past few years, interest in semiconductor oxides (SCOs) has grown significantly due to their adaptable technological applications [1,2]. Due to their non-toxic nature, stable chemical properties, and environmental benefits, they have been extensively studied as potential solutions to the mounting issues of environmental pollution and the energy crisis. SCOs can be used in a variety of applications, for instance, solar cells, UV–vis light emitters, fuel cells, batteries, transparent electronics, and photocatalysis [3–6]. The photocatalytic process encompasses light absorption, the generation and separation of electrons and holes, their transport to the photocatalyst's surface, and the subsequent redox reaction [7]. Semiconductor oxide (SCO)-based photocatalysis is a potentially transformative technology for addressing environmental and

* Corresponding author.
** Corresponding author. Department of Inorganic and Analytical Chemistry, Faculty of Chemical Technology and Biotechnology, Budapest University of Technology and Economics, Műegyetem rkp. 3, H-1111, Budapest, Hungary.
E-mail addresses: hamsasew.lemago@edu.bme.hu (H.H. Lemago), szilagyi.imre.miklos@vbk.bme.hu (I.M. Szilágyi).

https://doi.org/10.1016/j.mssp.2024.108733
Received 18 January 2024; Received in revised form 21 July 2024; Accepted 22 July 2024
Available online 1 August 2024

energy challenges and providing new opportunities in chemical synthesis and materials science because SCOs are highly photoactive and can be used to photocatalyze a broad range of reactions, such as, water-splitting, pollutant degradation, energy conversion, environmental remediation, and self-cleaning surfaces [8–10]. However, their photocatalysis efficiency is affected by many factors, including light absorption ability [2,11], band gap energy [12], interfacial electron transfer capacity [13], and recombination of photogenerated electrons and holes. Researchers are working to develop new SCO photocatalysts with improved efficiency and durability.

Zinc oxide is one of the most valuable n-type SCO photocatalysts [14] having an direct energy band (3.37eV) and high exciton binding energy (0.06eV) [15,16]. It is, as a material, finds applications in electronics [17], optoelectronics [18] and sensors [19]. However, its photocatalytic efficiency is yet challenging to meet the practical applications being used on a large scale commercially. These could be probably due to crystal structure [20], surface morphology [21], roughness [22], film thickness [25], and annealing temperature [25] of the ZnO nanostructure especially owing to its only UV absorbing feature. Developing ZnO with other oxides could be, therefore, more efficient to enhance photocatalysis. Efforts have been implemented in previous studies to improve the photocatalytic properties of ZnO nanostructures. These efforts encompass various approaches, including morphological engineering, metal dopants (Ag, Au, Cu) [26–28], composite formations like ZnO/TiO_2, WO_3/ZnO, CuO/ZnO and Al_2O_3/ZnO [29–33]. These composite material approaches boost photocatalytic performance by increasing the surface area of materials, narrowing band gap energy, improving light absorption, enhancing charge separation, and reducing electron-hole recombination.

Inverse opals represent a specific category of photonic crystals (PCs) that possess a three-dimensional arrangement of well-organized voids, interspersed by a network of interconnected spheres or solids. These structures display exceptional attributes, such as photonic bandgap (PBG), large surface area, adjustable optical, electronic, and mechanical properties, self-assembly capabilities, as well as plasmonic properties [34–36]. In the typical fabrication process of ZnO IO PCs, materials such as PS, polymethylmethacrylate, carbon nanospheres, or silica nanospheres are densely packed into a colloidal opal crystal lattice, which acts as a template. The voids within the template structure are then filled with ZnO, leading to the formation of a unique photonic crystal structure with advantageous optical and electronic properties. Eventually, the sacrificial templates are removed through calcination, while the silica colloids are dissolved using chemical etching with HF, resulting in the creation of the final ZnO IOPC [37,38].

Several infiltration techniques, including chemical vapor deposition [39], sol-gel, spin coating [40], hydrothermal [41], sputtering [42], and ALD [41], have been engineered to fabricate ZnO and composite nanostructures, with desirable characteristics. Among the mentioned techniques, ALD outstands as it enables the growth of ZnO layers that are uniform, conformal, and controlled at the atomic level on three-dimensional surfaces. ALD is experiencing rapid growth due to its advanced technology. It applies a vapor phase deposition method with self-regulated reactions, producing highly conformal and uniform thin films with sub-nanometer thickness [43–45].

Within the ALD family for depositing metal oxide thin films, two main approaches exist: thermal ALD (TALD) and plasma-enhanced ALD (PEALD). These methods differ significantly in their precursor activation, leading to contrasting film properties and material performance. TALD utilizes thermal energy (150 °C–400 °C) to activate precursors, driving reactions with the substrate surface. PEALD utilizes plasma (e.g., Ar, H_2, or O_2 radicals) for precursor activation. The lower operating temperatures (often below 100 °C) minimize damage, while the plasma bombardment promotes superior film conformity, resulting in smoother and more uniform surfaces. Additionally, studies show faster growth rates and higher growth per cycle for PEALD compared to TALD, potentially due to the more efficient plasma activation [46–48]. For example, when comparing the thermal and plasma-assisted ALD reactions for Al_2O_3, Trimethyl aluminum (TMA), H_2O, and O_2 radicals as precursors, the overall process into successive "half-reactions" as follows [49]:

Summary of TALD vs PEALD.

TALD reaction [50]	PEALD reaction [51,52]
Step-1: Surface reaction during TMA exposure TMA + Surface − OH → Surface-Al $(CH_3)_2$ + H_2O (g) **Step-2**: Surface reaction during H_2O exposure: H_2O + Surface − $Al(CH_3)_2$ → Surface-Al-OH + CH_4 (g) TMA + H_2O → Surface − Al–OH + CH_4	**Step-1**: Surface reaction during TMA exposure: TMA + Surface − H → Surface − Al $(CH_3)_2$ + CH_4(g) **Step-2**: Surface reaction during O_2 plasma exposure: $O^{\cdot}$ + Surface-$Al(CH_3)_2$ → Surface-Al-OH + CH_3OH(g) TMA + $O^{\cdot}$→ Surface − Al–OH + CH_3OH + CH_4

This study aims to synthesize and characterize pure ZnO and ZnO/Al_2O_3 composite structures using a combination of TALD and PEALD. First, a 51.4 nm thick ZnO layer was grown on a polystyrene (PS) nanosphere template using TALD. The ZnO layer was then annealed at high temperatures to form an IO structure. Next, an ultra-thin Al_2O_3 layer was grown on the ZnO IO structure using either TALD or PEALD. The PS colloid crystal template was fabricated using vertical layer deposition (VLD). The morphology, chemical composition, crystallographic structure, optical properties, and photocatalytic characteristics of the synthesized materials were explored in the presence of a variety of methodologies, including scanning electron microscopy-energy dispersive X-ray spectroscopy (SEM-EDX), XRD, Raman spectroscopy, spectroscopic ellipsometry, photoluminescence (PL) spectroscopy, and UV–Visible spectroscopy. The photocatalytic properties of the materials were also evaluated by exposing them to visible light irradiation for 3 h while using methylene blue (MB), Rhodamine 6G (Rh6G), and 4-Nitrophenol(4-NP) dyes as model pollutants.

2. Experimental procedures

2.1. Preparation of polystyrene (PS) nanosphere template: vertical layer deposition (VLD)

The preparation of a polystyrene (PS) suspension (Sigma Aldrich, 600 nm, 10 %) commenced with gently scraping powder from the PS bottle using a curved-end spatula. Subsequently, 15 mg of PS powder was mixed with 4.85 ml of ion exchange water and thoroughly stirred manually until a homogeneous dispersion was achieved (Fig. 2). To enhance particle uniformity and surface area, the suspension underwent high-frequency sonication treatment using Sono Plus equipment (Bandelin ultrasound, DIN EN 62638, Germany) with the following parameters: amplitude 30 %, pulsation time 0.5 s, energy 6.1 kJ, and duration 3 min at ambient temperature. Finally, the prepared PS suspension was utilized to grow an opal layer on a microscope glass slide using the VLD method, in line with our previous study protocol [53].

2.2. Atomic layer deposition: TALD/PEALD

Prior to TALD (Beneq, TFS-200-186) deposition, the ALD chamber was heated at 50 °C for 2 h, and then the opal samples and reference silicon wafer (100) were loaded together into the ALD reactor to begin the film growth process. Ultra-high purity nitrogen was used as the carrier gas, with a pressure of 6.8 mbar in the vacuum chamber and 1.4 mbar in the reactor. For ZnO thermal ALD deposition at 50 °C, diethyl zinc (DEZ), and H_2O precursors were used. The TALD process was conducted using a pulse/purge program that alternated between 300 m s of DEZ and 3000 m s of N_2, and 300 m s of H_2O and 3000 m s of N_2

(Schematic illustration is given in Fig. 1). A total of 539 ALD cycles were performed, resulting in a confirmed film thickness of 51.4 nm and a growth rate of 0.09 nm per cycle. An ultra-thin Al_2O_3 film layer was TALD deposited on top of the ZnO IO structure using a trimethyl aluminum (TMA) and H_2O precursors. The TALD process was conducted using a pulse/purge program that alternated between 150 m s of TMA and 3000 m s of N_2, and 150 m s of H_2O and 3000 m s of N_2. A total of 19 ALD cycles were performed, resulting in a film thickness of 4.4 nm (confirmed by ellipsometry) with a growth rate of 0.23 nm per cycle (Table 1).

On the other hand, the PEALD of Al_2O_3 on pure ZnO IO was performed using TMA and O_2 precursors. A constant radio frequency power of 50 W was applied to the plasma during PEALD to activate the O_2 oxidant. The vacuum chamber and deposition reactor maintained internal pressures of 7.4 mBar and 1.2 mBar, respectively. The sequence of pulses and purges was as follows: 150 m s of TMA, 2000 m s of nitrogen, 2000 m s of O_2 plasma, and 2000 m s of nitrogen. A total of 23 ALD cycles with plasma-assisted deposition produced a 5.5-nm-thick Al_2O_3 film with a growth rate of 0.23 nm per cycle.

2.3. Heat treatment of the samples: annealing and post-annealing

The heat treatment process involved placing both the samples and control samples into alumina ceramic crucibles to remove the template material. The process was carried out in a furnace in an air environment. In the heating program, the samples were heated from ambient temperature to 500 °C for 4 h and then maintained at that temperature for 2 h. After the PS template was effectively eliminated, the resultant structure comprised a high-quality pristine ZnO IO structure. Additionally, post-annealing was also carried out for composite materials using the same heating technique once Al_2O_3 had grown on the surface of IO structures. The annealing protocols proved highly effective in removing the template material and generating the IO structure.

2.4. Materials characterization

SEM analysis was performed utilizing a JEOL JSM-5500LV scanning electron microscope operating at 25 kV with an SEI Detector under high vacuum conditions. The samples were observed without any modification or treatment, and no conductive film (Au and Pd) was applied to prevent potential signal interference. EDX spectra were captured using the JEOL JSM-5500LV SEM, with three measurement points taken for each sample and an average of them.

The structural analysis was performed using a PAN analytical X'Pert Pro Monochromatic Parallel-Beam Powder XRD with Copper K-alpha (λ = 1.540 Å) radiation, in the 2-Theta (5–70°). These patterns were compared to the reference to identify the crystalline phases present in the materials. The mean size of the crystallites, D, was determined with the Scherrer equation:

$$D = \frac{K\lambda}{\beta\, Cos\, \theta} \tag{1}$$

Where K is the constant, λ is the wavelength of the radiation, β is the full width of diffraction peaks at half-maximum (FWHM), and θ is the angle at which the peak occurs (Bragg angle).

The photonic bandgap (PBG) of the IO materials has been estimated by using a modified Bragg's equation (2), shown below [20,34]:

$$\lambda_{max} = 1.632D\left(n_{avg}^2 - Sin^2\theta\right)^{1/2} \tag{2}$$

Where λ_{max} is the wavelength of the band maximum (PBG) of the materials, D is the diameter of spheres (would generally be taken as 2r, where r is the sphere radius.), θ is the angle between the incident light and the surface of the sample. The average refractive index n_{avg} of the samples can be calculated using the following equation (3):

$$n_{avg} = f_{sphere}\, n_{sphere} + \left(1 - f_{sphere}\right) n_{air} \tag{3}$$

Where f_{sphere} is the filling factor, representing the proportion of space occupied by the solid PS spheres within the overall structure. For a face-centered cubic lattice, the volume fractions of PS spheres and air f_{air} is typically 74 % and 26 %, respectively. Additionally, n_{PS}, n_{ZnO}, n_{Al2O3}, and n_{air} represent the refractive indices of PS, ZnO, Al_2O_3, and air, respectively. The refractive indices are: $n_{PS} = 1.59$, $n_{ZnO} = 2.0$, $n_{Al2O3} = 1.7$, and $n_{air} = 1.0$.

The Raman structural analysis was done using a Jobin Yvon Labram Raman spectrometer equipped with an Olympus microscope and a green Neodymium-doped Yttrium Aluminum Garnet laser. The Raman shift (in wave number) was measured within the range of 100–1800 cm^{-1}.

UV–Vis spectroscopy of the samples was conducted using an

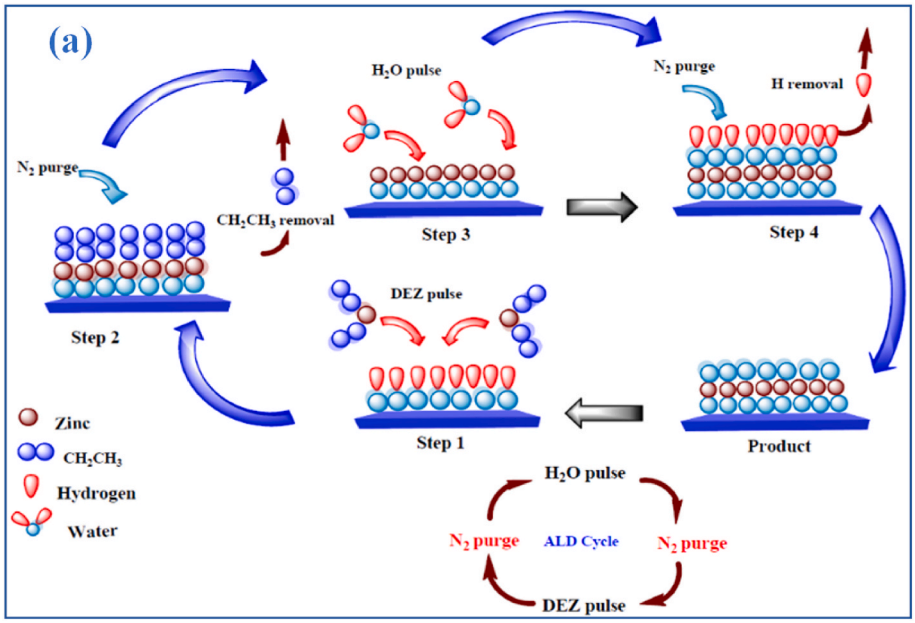

Fig. 1. Graphic representation of the ALD reaction for ZnO using DEZ and H_2O precursors.

Table 1
ALD reaction parameters.

Sample Name	Deposited oxides	Modes of ALD reaction	Temp. (^{0}C)	ALD cycles	Thickness (nm)	GPC (nm)
ZnO	ZnO	T	50	539	51.4	0.09
ZnO/Al_2O_3-T	Al_2O_3	T-T	50	19	4.4	0.23
ZnO/Al_2O_3–P	Al_2O_3	T-P	50	23	5.5	0.23

"T" stands for thermal; and "P" stands for plasma.

AvaSpec-2048 spectrometer from AVANTES, equipped with an Ava Light-DHS deuterium halogen lamp. Ava Soft software was used for absorbance-reflectance-mode data acquisition.

A SEMILAB Spectroscopic Ellipsometer SE-2000 (Cambridge, USA) was utilized to measure the thickness of the IO films and reference samples. To ensure accurate measurements, reference Si (100) wafers were integrated as control samples in the ALD system along with the opal and IO samples.

PL spectra were obtained using an Edinburgh Instruments Fast spectrum (FS) 5 spectrofluorometer, employing an excitation wavelength of 380 nm at 25 °C and a long pass glass filter in the emission beam at 380 nm.

To assess the photocatalytic performance of ALD-grown materials, they were subjected to visible light irradiation while immersed in solutions containing MB, Rh6G, and 4-NP dyes for 3 h. Each sample was attached to the walls of a glass vessel using plastic tape, ensuring that only the film portion was fully submerged in the 10 mL each of 5.0×10^{-6} M, 3.8×10^{-6} M Rh6G, and 8.5×10^{-6} M 4-NP (pH = 10.01 buffer) dye solutions. Prior to irradiation, the samples were kept in the dark for 30 min to allow adsorption-desorption equilibrium to establish. At regular intervals of 30 min, 3 ml of the solution was carefully pipetted into a quartz cuvette and its absorbance was measured using an Avantes fibre optic spectrometer (AvaSpec-2048) equipped with an Ava Light-DHS light source. The absorbance readings were transformed into dye concentration values. The photocatalytic decomposition of the dyes was initiated by exposing the sample solutions to visible light irradiation from three Osram 18 W lamps arranged in a stack configuration. The sample solution was placed in front of the central lamp and maintained at 5 cm to guarantee uniform lighting conditions. This experimental setup enabled the quantification of the photocatalytic activity of the ALD-grown samples over time, providing insights into their efficiency in degrading MB(λ_{max} = 665 nm) and Rh6G(λ_{max} = 527 nm), 4-NP(λ_{max} = 400 nm) under visible light irradiation.

3. Results and discussion

Fig. 2 describes the process of fabricating the periodically ordered IO structure of pristine ZnO and ZnO/Al_2O_3 composite materials using thermal and PEALD techniques, combined with the VLD method. This technique was used to grow the colloid crystal template on the glass slides. The process began with the proper dispersion of PS powder to form aggregates, as illustrated in (Fig. 2) in path "a to d". Subsequently, the template was subjected to low-temperature (50 °C) TALD infiltration of ZnO followed by annealing at a high temperature of 500 °C, resulting

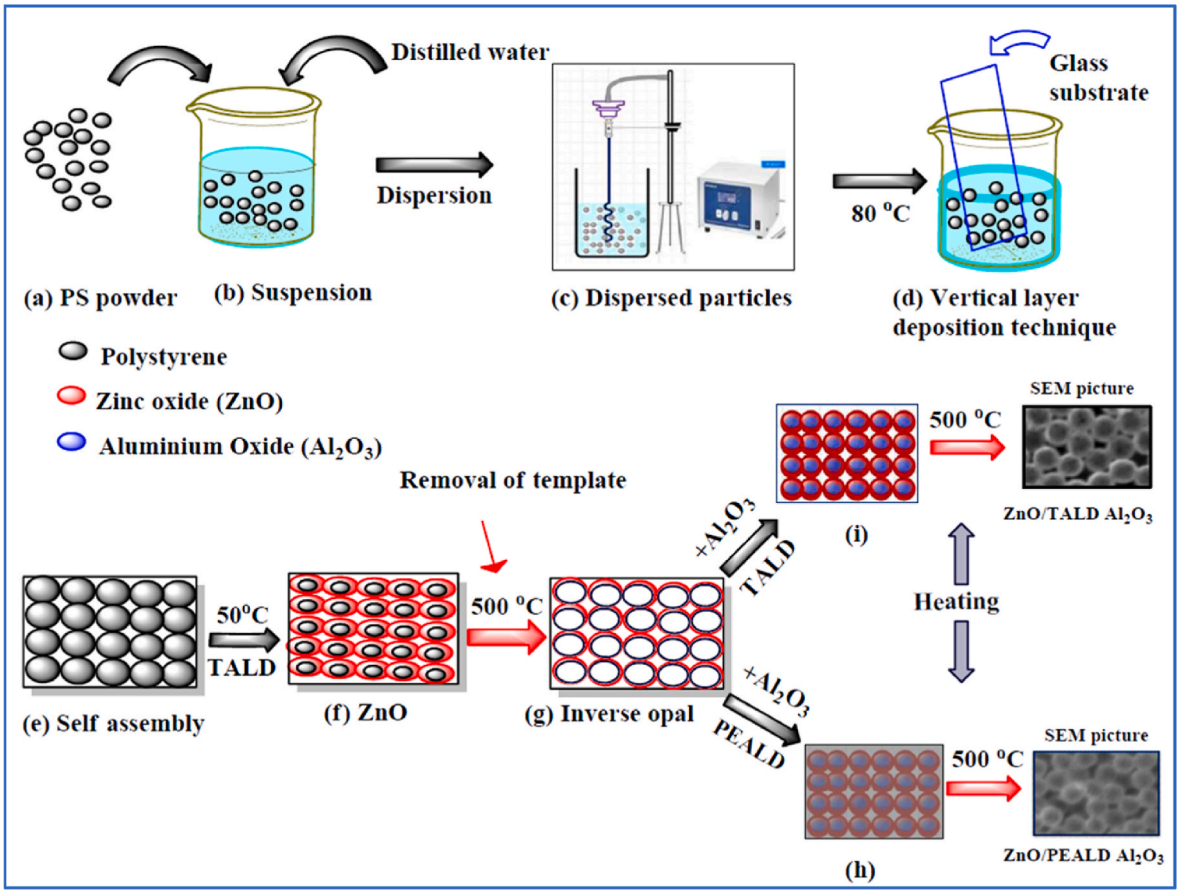

Fig. 2. Fabrication schemes of ZnO IO and ZnO/Al_2O_3 nanocomposite structures using TALD and PEALD techniques.

in the IO structure (see path "e"). The final synthesis pathway shows (route "h and i"), that Al_2O_3 thin films were grown onto the original IO structure using TALD and PEALD techniques. Subsequently, another annealing step was conducted, resulting in the formation of a composite nanomaterial composed of ZnO/Al_2O_3.

3.1. SEM study

Fig. 3a–h presents SEM images of the ALD-grown samples captured at high magnifications. A high-quality colloidal crystal template (Fig. 3a–b), comprising colloid nanospheres with a size of ~588 nm (SEM measurement), was synthesized using the VLD technique. The top view SEM images clearly exhibited a periodic arrangement of monodispersed colloidal spheres, with a close-packed plane, like the (100) planes of a face-centered cubic (FCC) crystal network. These template structures have shown promising potential as suitable candidates for ALD infiltration techniques. Fig. 3c–d shows a clear image of a unique hollow structure of a pristine ZnO IO with a thickness of approximately

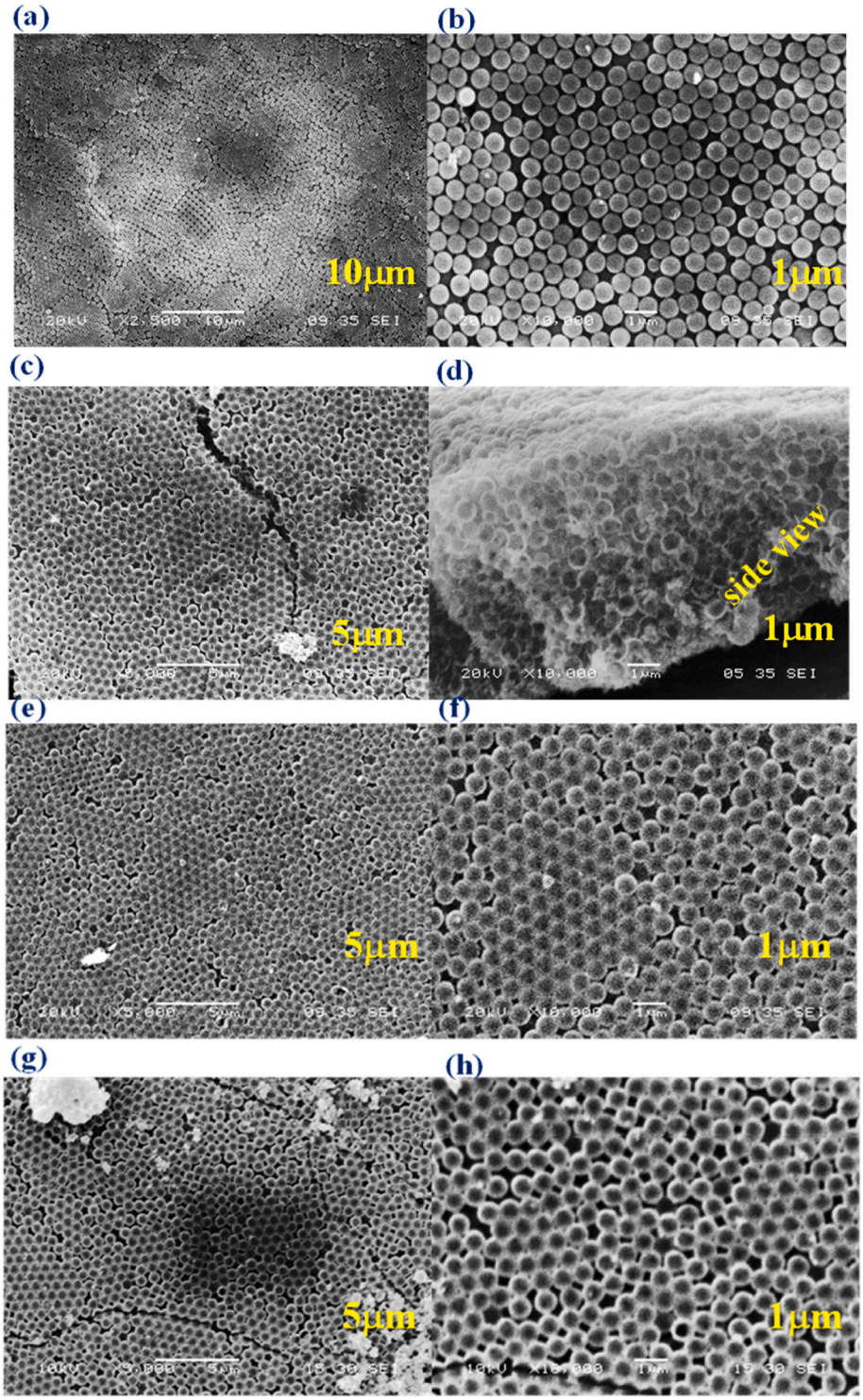

Fig. 3. SEM images of the ALD sample: (a–b) PS template, (c–d) ZnO IO synthesized by TALD, (e–f) ZnO/Al_2O_3-T composite sample, and (g–h) ZnO/Al_2O_3–P composites respectively.

51.4 nm, as confirmed by Ellipsometry (Table 1). This structure is made up of interconnected spheres that follow the template morphology. Composite IO architectures deposited through TALD yielded uniform, ordered spheres. However, PEALD deposits exhibited slightly lower periodicity and less order compared to their TALD counterparts (Fig. 3e–h). The composite structures grown through TALD-Al_2O_3 exhibited nearly equivalent high levels of ordering when compared to the PEALD-Al_2O_3 structure. It is evident that a 5 nm ALD deposition did not change the overall surface morphology of the pure IO structure, thereby preserving its remarkably uniform and conformal ALD coating [54]. Annealing and post-annealing temperature were sufficiently high to eliminate the template without altering its IO and composite structure, while the deposition temperature remained notably lower. Furthermore, annealing the sample at 500 °C resulted in shrinkage of the sphere size for all materials. The volume shrinkage, estimated by SEM analysis (Table S1), was 8.0 % for ZnO IO, 16.7 % for ZnO/Al_2O_3-T, and 15.2 % for ZnO/Al_2O_3–P. This higher shrinkage in the composites compared to the pure IO structure is likely due to the double-step heat treatment.

3.2. EDX study

EDX analysis confirmed the successful deposition of ZnO and Al_2O_3 using either TALD or PEALD techniques (Figs. S1a–c). Pristine ZnO IO comprised Zn and O in a near stoichiometric ratio. However, PEALD results in greater deposition of Al_2O_3 (9.8 %, At) compared to TALD (8.4 %, At) in the composite materials (Fig. S1d). EDX analysis also detected minor quantities of C attributed to residual precursors, as well as of Na, Al, Si, and Ca, originating from the glass substrate.

3.3. Raman study

Raman analysis confirmed the wurtzite crystalline nanostructure of the pure IO, with the most prominent peak at ~433 cm^{-1} and shifts at ~333, ~436, ~578, ~995, and ~1132 cm^{-1} (Fig. 4a). The composite samples made of Al_2O_3 either TALD or PEALD did not show any Raman shifts, and their peak intensities varied, with PEALD having a lower intensity than TALD. This is mainly because the Al_2O_3 samples were too thin to be detected by Raman due to the limited number of ALD cycles used (19 for thermal and 23 for plasma modes). Previous studies have indicated that the formation of crystalline α-Al_2O_3 and γ-Al_2O_3 films through ALD requires a greater number of ALD cycles and higher annealing temperatures (exceeding 1000 °C) [55].

3.4. XRD study

From XRD analysis (Fig. 4b) it can be observed that all major peaks were indexed with a hexagonal wurtzite crystal ZnO IO structure that matched very well with the standard data (ICCD card Number: 98-016-1836). The pure IO and TALD composite exhibited similar crystallite sizes of 37.4 nm as determined by the Scherrer equation in Table 2. This implies that both materials possess a higher porosity and surface area, attributed to the larger crystallites allowing for more space between the crystal grains. However, the 5 nm Al_2O_3 layer grown on IO structure using either TALD or PEALD was too thin and amorphous to be detected by XRD.

Due to the fragility of PS nanosphere templates and the destruction of IO structures at high annealing temperatures, the Al_2O_3 ALD film can only be crystallized by annealing at 1000–1200 °C [56]. Hence, annealing the TALD composite at 500 °C further increased the order of the ZnO IO (Fig. 4b) structure but annealing the PEALD composite at 500 °C was not enough to restore the ZnO order. PEALD-coated composite disrupted the order of ZnO IO, leading to stronger XRD peaks for TALD composites. In contrast, the PEALD-coated ZnO IO composite showed a larger crystallite size of 63.55 nm (Table 2), suggesting disordered growth. This difference is due to the distinct ALD mechanisms of TALD and PEALD.

3.5. UV vis absorption study

This studies revealed that all three samples showed a sharp drop in absorption at around 400 nm, which is the absorption edge of ZnO semiconductors [41,57]. The pristine IO exhibited the strongest UV light absorption between 360 and 380 nm (Fig. 5a), which matches the fundamental band gap of ZnO, likely due to quantum confinement effects in the IO. The calculated band gap of ZnO IO was 3.3 eV (Fig. S2), which matches with bulk ZnO (3.2 eV) [58]. ZnO–Al_2O_3 composites have a similar absorption threshold (edge) at 400 nm as pure ZnO, even though Al_2O_3 nanoparticles have UV absorption at ~280 nm [59]. This

Table 2
Crystallite sizes.

Sample	Peak position-2 θ (^{0})	FWHM	Crystallite sizes/nm
ZnO	33.9	0.26	37.4
ZnO/Al_2O_3-T	33.9	0.26	37.4
ZnO/Al_2O_3–P	32.5	0.14	63.5

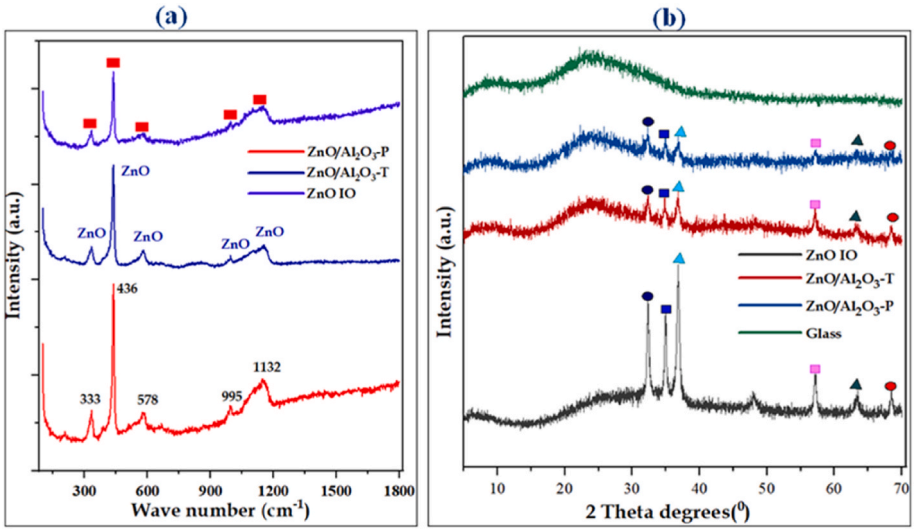

Fig. 4. (a) Raman spectroscopy, and (b) XRD diffraction patterns.

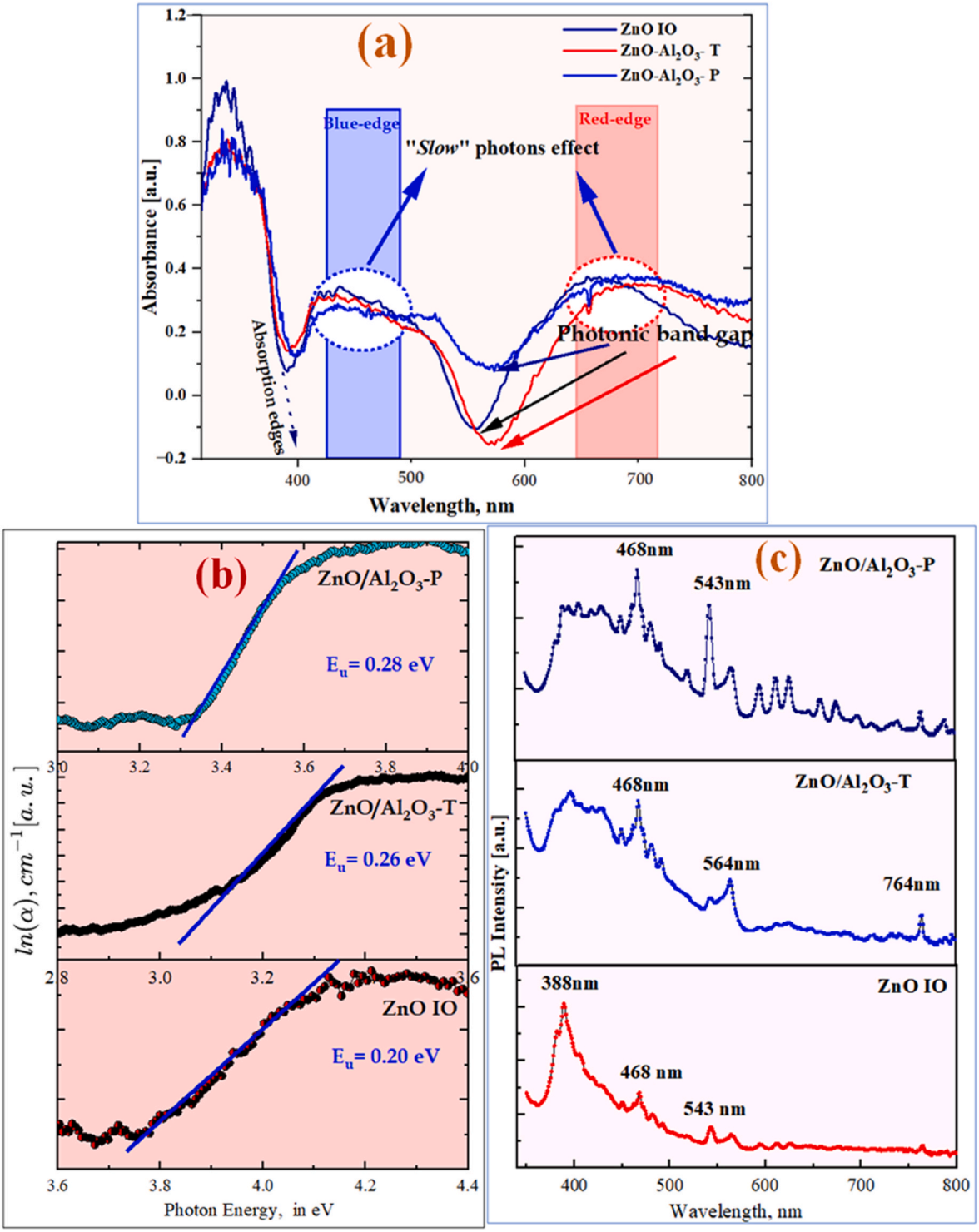

Fig. 5. (a): UV Visible absorption spectroscopy, (b): The Urbach energy (E_u) values of the samples, and (c) The PL emission spectra of the ALD samples: uncoated ZnO IO, composite ZnO–Al_2O_3-T, and composite ZnO–Al_2O_3–P respectively.

is because the Al_2O_3 layer in the composites is very thin, so its effect on the overall absorption spectrum is insignificant. The ZnO IO structure also exhibited two absorption peaks at wavelengths of 434 nm (blue edge) and 660 nm (red edge), indicating enhanced photon absorption "slow photon effect" at the edges of the PBG centered at 560 nm, which was dictated by the size of the sacrificial template (588 nm). Based on the modified Bragg's estimation, the theoretical PBG of the ZnO IO structure falls within the visible region at approximately 676 nm (See Table S1). The two absorption peaks in the IO structure match to the wavelengths of light where the light waves are slowed down the most because when light travels through an IO structure, it slows down as it interacts with the periodic structure of the IO material. At these wavelengths, the light waves are more likely to be absorbed by the IO material [60,61].

The composite (Fig. 5a) had two absorption peaks in the visible region, similar to the pure IO, but their PBGs were slightly shifted to 580 nm and 570 nm for the TALD and PEALD composites, respectively. This suggested that the Al_2O_3 was also slightly shifting the PBG of the ZnO IO.

However, the calculated PBGs (557 nm for ZnO/Al_2O_3-T and 565 nm for ZnO/Al_2O_3–P) deviated from experimental values, being lower than bare ZnO IO (Table S1). The different PBGs of the pure ZnO IO and the composite structures are likely due to their macrostructural differences. Al_2O_3 deposition had further changed band gap energies of PEALD (3.4 eV) composite (Fig. S2) possibly due to defects introduced by the ultra-thin Al_2O_3 layer that trapped electrons and holes [31]. The pure IO has an ordered structure, while the composite structures have a slightly ordered structure. This difference in order may affect how light propagates through the materials, and thus affect the PBG.

Urbach energy (E_u) is a measure of structural disorder in nanostructures, caused by oxygen vacancies and defect states that capture electrons and narrow the band gap [62,63]. It is calculated by plotting ln (α) vs. photon energy (hv) and measuring the slope of the linear region, with the E_u having the opposite sign of the slope. The absorption coefficient (α) is related to the disorder according to the following equation: [64,65].

$$\alpha = \alpha_o \, exp[hv / E_u] \tag{4}$$

where, α_o is constant.

For all sample materials the calculated E_u values were 0.20, 0.26, and 0.28 eV, as Urbach band tails, respectively (Fig. 5b). The Al_2O_3-coated IO structure had a higher E_u value than the uncoated ZnO counterpart, which meant that the Al_2O_3 coating had introduced disorder into the ZnO IO layer. The observed increase in the E_u value was due to the structural defects introduced into the crystal lattice by the plasma-enhanced techniques. Therefore, the ZnO/PEALD-Al_2O_3 sample exhibited a greater degree of disorder and had the potential to create oxygen vacancies within the Al_2O_3 when compared to the ZnO/TALD-Al_2O_3 or uncoated-ZnO IO structures [65,66].

3.6. PL studies

The PL properties of ALD samples were illustrated (Fig. 5c). Pure ZnO IO emitted light in both UV region and visible region respectively, but the composites were only emitted light in the visible range. The pure inverse opal (IO) structure exhibited a prominent ultraviolet (UV) emission peak at 388 nm in its photoluminescence (PL) spectrum, which was ascribed to the direct recombination of charge carriers. It also had small peaks in the visible region at 468 nm (blue emission) and 543 nm (green emission), explained by the relaxation of electrons trapped at surface defects [67,68]. The ZnO–Al_2O_3-T composite exhibited a few peaks at 468 nm, 564 nm, and 764 nm, while the PEALD composite exhibited two sharp peaks at 468 nm and 543 nm, as well as several small multiple peaks at 569 nm, 596 nm, 613 nm, 628 nm, 659 nm, and 679 nm. Hence, the PEALD composite emitted more visible light than the TALD, due to the formation of more defects at the ZnO–Al_2O_3 interface, which acted as traps for charge carriers and promoted their recombination in the visible region [69]. The TALD composite, on the other hand, has fewer defects overall, which leads to lower visible light emission but higher photocatalytic activity. The PL emission can be attributed to the recombination of charge carriers, most likely stemming from defects within the inverse opal structure, potentially originating from plasma depositions.

3.7. Photocatalytic studies

3.7.1. Degradation of dyes using visible light irradiation

The photocatalytic activity of the samples was evaluated by the relative absorbance of the dyes. The relative absorbance (A_0/A_t) of the materials were calculated using equation (5):

$$A_0 \Big/ A_t = 1 - \frac{At}{Ao} \tag{5}$$

where A_o is the initial absorbance of dyes and A_t is the absorbance after irradiation time t. A pseudo-first-order equation was used to determine the rate constant of the dye degradation in the sample solution:

$$\ln[C_o / C_t] = kt \tag{6}$$

where k is the rate constant. C_o is the initial concentration of dyes and C_t is the concentration after irradiation time t. The linear plots of -ln (C_o/C_t) versus irradiation time, t, were shown in (Fig. 7a–c), and the calculated rate constants were provided in Table 3.

All samples successfully decomposed the dye solution after being exposed to visible light for 3 h. Without a catalyst, the dyes relative absorbance was evaluated to be only 0.04 for MB, 0.02 for Rh6G, and 0.02 for 4-NP respectively (Fig. 6a–c), over 3 h using Equation (4) and showed a lower rate constant in Fig. 7a-c. This indicates that dye solutions were stable and resistant to degradation without a catalyst. Moreover, this study also investigated the photodegradation kinetics of ALD photocatalysts against MB, Rh6G, and 4-NP dyes. All samples showed pseudo-first-order degradation kinetics (details in Table 3).

The pristine IO structure demonstrated the most effective photocatalytic performance in degrading MB, evidenced by its relative absorbance of 0.42 (Fig. 6a). This was attributed to the highly ordered IO structure's ability to efficiently capture and guide light into deeper layers of the material, allowing for the breakdown of dye molecules [20,70,71]. However, the same structure exhibited reduced efficiency in degrading Rh6G dye, with a relative absorbance of 0.72 (Fig. 6b). Additionally, the large pore size of the template (~588 nm) generated a pronounced slow light effect, further enhancing light absorption. In comparison to both MB and Rh6G dyes, 4-Nitrophenol exhibited the slowest degradation kinetics. Its relative absorbance was measured at 0.78, and its rate constant was slower than that of Rh6G and MB dyes.

This study demonstrated that a photocatalyst with an IO structure coated with an ultra-thin layer (4.4 nm thick) of Al_2O_3 thermally deposited exhibited superior photocatalytic performance compared to pure IO and ZnO/Al_2O_3–P composites. The TALD-coated IO achieved the fastest degradation rate (k up to 0.0022 min^{-1}) and efficiency (up to 69 %) for MB and Rh6G dyes, surpassing PEALD and pure IO by at least 10 %. However, degradation of 4-NP was slower (k = 0.0011 min^{-1}). This enhanced photocatalytic performance could be attributed to three main factors: (i) the ultra-thin Al_2O_3 layer acted as a passivation layer, preventing the recombination of photogenerated charge carriers, allowing them to participate in more chemical reactions and effectively decompose dyes; (ii) the TALD method successfully preserved the highly IO ordered structure after annealing, creating a photonic crystal that controlled light interaction. Tailoring the PBG and utilizing the slow light effect enhanced light absorption across a broad spectrum. This increased light capture significantly boosted the generation of reactive oxygen species, promoting efficient dye degradation through photocatalysis, and (iii) the controlled number of defects (E_u = 0.26 eV) introduced by TALD, confirmed by PL, created new energy states in the bandgap, enabling the photocatalyst to absorb light over a wider wavelength range.

Furthermore, according to Table 3, the k values of the ZnO/Al_2O_3-T composite varied for the three dyes because of their interaction with visible light. MB possessed a conjugated chromophore structure [72] that efficiently absorbed visible light, leading to the excitation of electrons into higher energy levels. Upon excitation, these electrons readily transferred to the CB of the ZnO/Al_2O_3-T composite, generating a positive hole (h^+) in the VB. Like MB, Rh6G also contained a conjugated chromophore [73,74] system allowing visible light absorption. However, the specific structure of Rh6G might have led to a slightly less efficient transfer of excited electrons to the ZnO/Al_2O_3-T compared to MB, explaining its slower degradation rate. Unlike MB and Rh6G, 4-NP had a simpler structure with a chromophore that was absorbed primarily in the UV region [33]. This limited visible light absorption translated to a lower degradation rate of electron excitation and subsequent charge separation in the ZnO/Al_2O_3-T composite.

Table 3
Rate constant and R-squared of sample in dyes.

Sample	MB		Rh6G		4NP	
	$kx10^{-2}(min^{-1})$	R^2	$kx10^{-2}(min^{-1})$	R^2	$kx10^{-2}(min^{-1})$	R^2
ZnO IO	0.19	0.9993	0.17	0.9993	0.11	0.9991
ZnO/Al_2O_3-T	0.22	0.9995	0.19	0.9994	0.15	0.9984
ZnO/Al_2O_3–P	0.11	0.9975	0.10	0.9966	0.10	0.9996

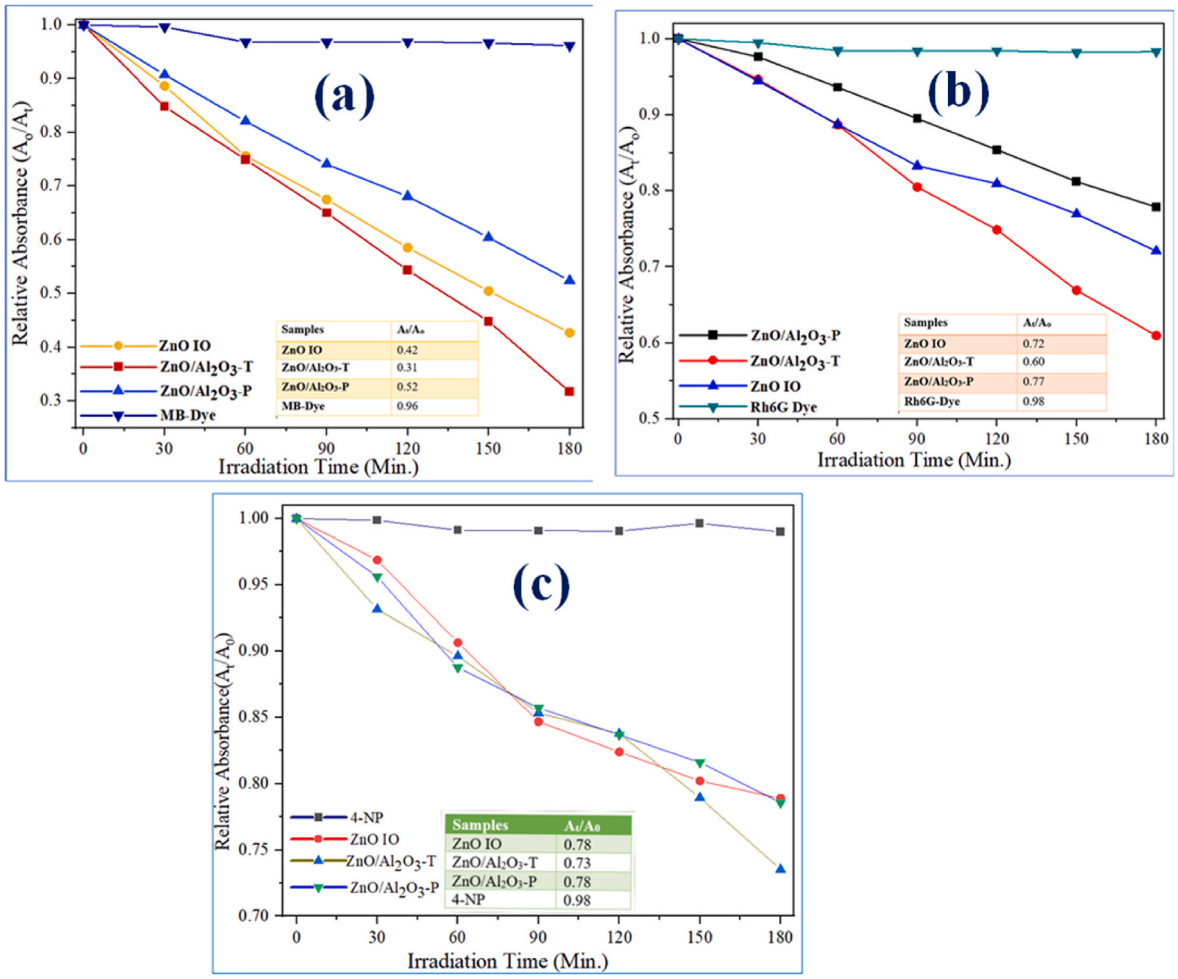

Fig. 6. Decolorization of MB, Rh6G, and 4-NP dyes through photocatalysis under visible light irradiation for 3 h using photocatalyst samples grown through ALD. (a–c) Photocatalytic performance – A_t/A_0 vs irradiation time, using ALD photocatalyst samples in the presence of MB(a), Rh6G(b), and 4-NP(c), respectively.

The PEALD-coated ZnO–Al_2O_3 composite sample showed reduced photocatalytic performance due to the plasma-assisted deposition process, which caused the composite material to become slightly amorphous characteristics. Moreover, the composites also exhibited slower degradation rates, k, compared to the TALD-coated IO composite for all three pollutants (MB, Rh6G, and 4-NP) as shown in the table. Therefore, the PEALD deposition process reduced the order of the ZnO IO to a less crystalline IO structure. Additionally, this mode generated a higher defect level, as indicated by a greater Urbach energy ($E_u = 0.28$ eV) and increased ($E_g = 3.4$ eV) compared to its TALD ($E_g = 3.3$ eV) counterpart or uncoated ZnO IO. Consequently, these factors collectively influenced the degradation of dyes, resulting in reduced photocatalytic activity. Even though Al_2O_3 deposition using PEALD at an ultra-thin level showed reduced photocatalysis here, it has a promising photolysis result achieved in recent studies reported by Shenoda et al. [75]. The report presented that enhancing the photocatalytic activity by decreasing the thickness decreases the band gap energy.

3.7.2. *Mechanism of dye degradation (ZnO–Al_2O_3-T material)*

Upon absorbing visible light, pristine ZnO IO ($E_g = 3.3$ eV) excited electrons into its CB and left holes in its VB. While bulk Al_2O_3 typically acted as an insulator due to its wide band gap, the ultra-thin films used in this study (grown by TALD/PEALD) were neither bulky nor crystalline. Recent research demonstrated that these 8 nm thick, amorphous PEALD-grown Al_2O_3 films possessed a narrower band gap ($E_g = 4.3$ eV) and contained excess oxygen vacancies, creating beneficial defect levels within the band gap for photocatalysis. These vacancies played a crucial role by suppressing the recombination of photo-generated charge carriers and extending their lifetimes. The Al-rich nature of the ALD-grown Al_2O_3 layer was believed to be the source of these excess oxygen vacancies [75,76].

ZnO/Al_2O_3 composite improves photocatalytic efficiency by

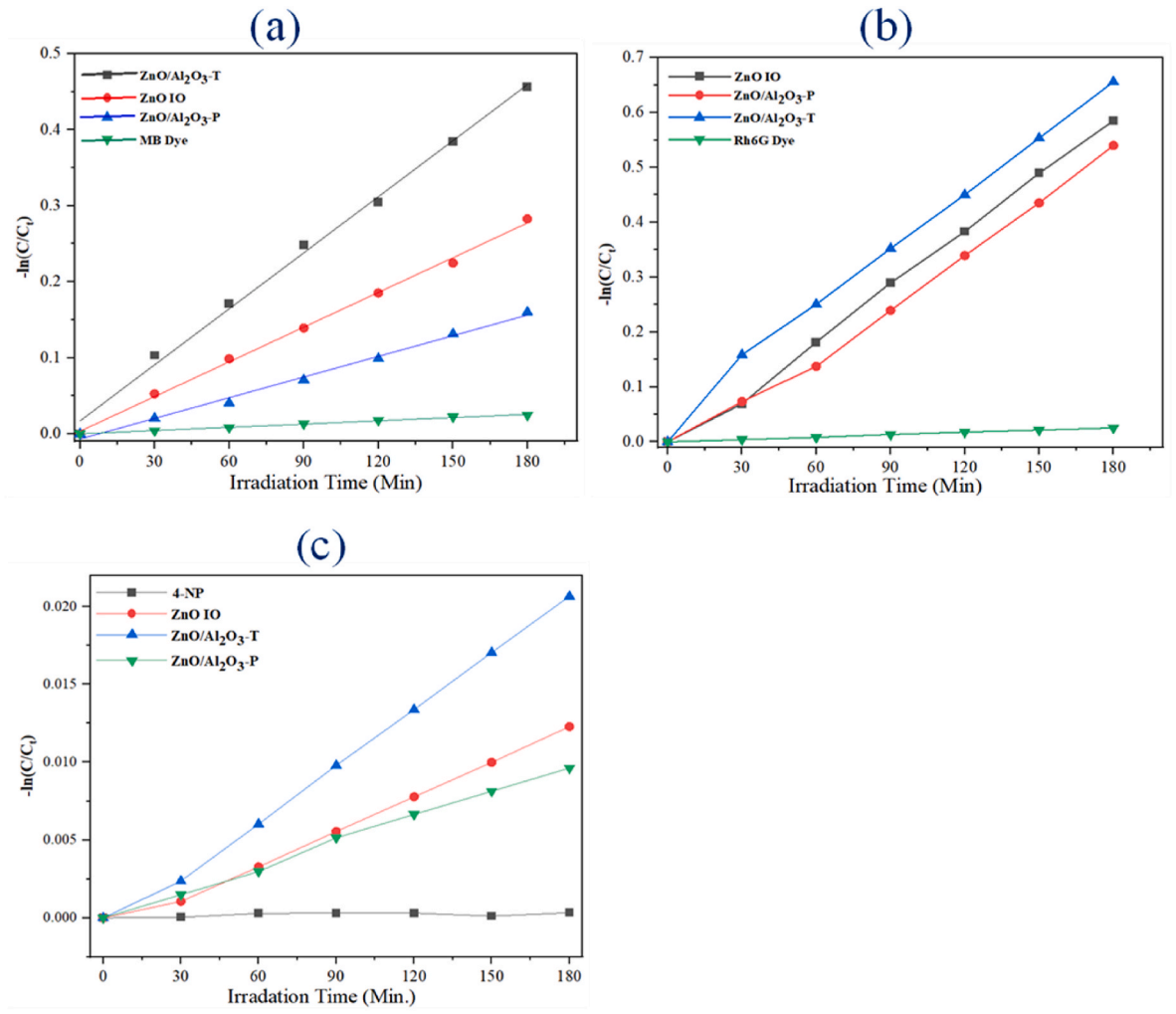

Fig. 7. (a–c) The pseudo-first-order linear plots of ln (C_o/C_t) versus irradiation time, illustrating the reaction kinetics for all sample materials.

suppressing charge recombination. An ultra-thin TALD Al_2O_3 layer acts as a passivating layer, reducing recombination and allowing more charge carriers to participate in redox reactions. The TALD processes facilitated this by creating an intimate interface between the ZnO IO and the ultra-thin Al_2O_3 layer, enabling efficient separation of photo-generated charges. This optimized light interaction could have enhanced light path lengths and improved light absorption by ZnO, allowing it to degrade a wider range of pollutants. The favorable band alignment in ZnO/Al_2O_3 further promoted electron transfer, reduced recombination, and extended charge carrier lifetime. These separated charges (e^-/h^+) drove photocatalytic reactions, degrading organic pollutants and generating radicals (O_2^-/•OH) for further degradation [31, 77–79].

4. Conclusions

In this study, we used ALD to synthesize pure ZnO IO and ZnO–Al_2O_3 composites on vertically deposited PS nanosphere templates. The PS sacrificial templates were thermally eliminated at 500 °C to obtain the IO microstructures. Ultrathin Al_2O_3 layers were then deposited on the IOs using TALD and PEALD methods. This approach yielded high-quality ZnO IO and ZnO–Al_2O_3 composites with uniform morphologies and precisely tailored compositions. SEM analysis confirmed that the monodispersed, and uniform colloidal nanosphere template was self-assembled to the FCC plane (a closed-packed plane) on a glass substrate. All SEM, XRD, and Raman results confirmed the formation of periodically arranged spheres with a hexagonal wurtzite phase ZnO IO structure and that the Al_2O_3 layer is too thin to be detected by Raman or XRD. Annealing the TALD composite at 500 °C further increased the order of the ZnO IO structure but annealing the PEALD composite at 500 °C was not enough to restore the ZnO order. The EDX analysis results confirm that the TALD and PEALD methods can be used to successfully deposit ZnO and ZnO–Al_2O_3 composites. All three materials (pristine IO, TALD composites, and PEALD composites) exhibited strong absorption of UV light due to the bandgap of ZnO. The pristine ZnO IO structure displayed enhanced absorption of light at specific visible wavelengths ("slow photon effect") because of its periodically arranged IO structure. The addition of Al_2O_3 to the composites caused a slight shift in the absorption peaks and resulted in higher calculated bandgaps compared to pure IO. These changes were likely caused by modifications in the structure and the formation of defects. Furthermore, E_u for the composites, Al_2O_3-coated IO structures than for the uncoated ZnO IO counterpart. This meant that the Al_2O_3 coating had also introduced disorder into the ZnO IO layer. The PL properties of ALD samples were also shown. Pure ZnO IO emitted light in both ranges, but the ZnO–Al_2O_3 composites only emitted light in the visible range. The PEALD composite emitted more visible light than the TALD, due to the formation of more defects at the ZnO–Al_2O_3 interface. In terms of photocatalytic activities of samples, pure ZnO IO excelled at degrading MB due to its light absorption and large pores, but its performance dropped significantly with Rh6G and nearly stalled with 4-NP. Remarkably, incorporating an ultra-thin layer of Al_2O_3 via TALD (ZnO/Al_2O_3-T)

significantly improved photodegradation across all dyes. This enhancement is attributed to the ability of the TALD process to not only suppress charge recombination and maintain the crystalline structure of ZnO IO but also potentially manipulate light interaction within the IO structure. This photonic effect, arising from the periodic arrangement of voids in the ZnO IO, could lead to optimized light scattering and enhanced light path lengths within the material, promoting more efficient dye degradation for a wider range of pollutants. In contrast, the PEALD process resulted in a less crystalline and defect-ridden ZnO–Al_2O_3 composite, crippling its photocatalytic activity.

CRediT authorship contribution statement

Hamsasew Hankebo Lemago: Writing – original draft, Software, Methodology, Investigation, Funding acquisition, Formal analysis, Data curation, Conceptualization. **Nour Khauli:** Methodology, Investigation, Formal analysis, Conceptualization. **Dóra Hessz:** Methodology, Investigation, Formal analysis, Conceptualization. **Tamás Igricz:** Methodology, Investigation, Formal analysis, Conceptualization. **Pál Petra:** Methodology, Investigation, Formal analysis. **Csaba Cserháti:** Methodology, Investigation. **Baradács Eszter Mónika:** Methodology, Investigation, Formal analysis. **Bence Parditka:** Methodology, Investigation, Formal analysis, Data curation. **Zoltán Erdélyi:** Writing – review & editing, Supervision, Software, Resources, Formal analysis, Conceptualization, Methodology, Investigation, Formal analysis. **Imre Miklós Szilágyi:** Writing – review & editing, Supervision, Formal analysis, Data curation, Conceptualization.

Declaration of competing interest

The authors have no financial relationships with any companies whose products or services are mentioned in this article. The authors have no patents, trademarks, licensed technologies, or copyrights that could be affected by the publication of this article. The authors have no personal relationships with any individuals whose interests could be affected by the publication of this article.

Data availability

Data will be made available on request.

Acknowledgments

The research conducted at BME and reported in this paper was supported by the NRDI Fund (TKP2021 BME-NVA), which was granted by the NRDI Office under the Ministry for Innovation and Technology. Additionally, project no. TKP2021-NKTA-34 was implemented with the support of the Hungarian National Research, Development and Innovation Fund (NKFIH) under the grant scheme OTKA K143724 and the TKP2021-NKTA funding scheme. The study was further supported by SH Hungarian government scholarship.

The authors would like to express their gratitude to Budapest University of Technology and Economics, the University of Debrecen, and the Tempus Public Foundation for providing valuable online resources, comprehensive databases, and laboratory facilities.

Appendix A. Supplementary data

Supplementary data to this article can be found online at https://doi.org/10.1016/j.mssp.2024.108733.

References

[1] J. Theerthagiri, S.J. Lee, K. Karuppasamy, S. Arulmani, S. Veeralakshmi, M. Ashokkumar, M.Y. Choi, Application of advanced materials in sonophotocatalytic processes for the remediation of environmental pollutants, J. Hazard Mater. 412 (2021) 125245, https://doi.org/10.1016/j.jhazmat.2021.125245.

[2] C. Karthikeyan, P. Arunachalam, K. Ramachandran, A.M. Al-Mayouf, S. Karuppuchamy, Recent advances in semiconductor metal oxides with enhanced methods for solar photocatalytic applications, J. Alloys Compd. 828 (2020) 154281, https://doi.org/10.1016/j.jallcom.2020.154281.

[3] L. Zhu, X. Shang, K. Lei, C. Wu, S. Zheng, C. Chen, H. Song, Doping in semiconductor oxides-based electron transport materials for perovskite solar cells application, Sol. RRL 5 (2021), https://doi.org/10.1002/solr.202000605.

[4] A. Chaudhari, X. Cui, B. Hoex, L. Hyde, C.N. Ironside, W.M. Jadwisienczak, M. E. Kordesch, F. Rahman, R.D. Vispute, Zinc oxide family semiconductors for ultraviolet radiation emission – a cathodoluminescence study, Mater. Res. Bull. 153 (2022) 111906, https://doi.org/10.1016/j.materresbull.2022.111906.

[5] Y. Yu, S. Hu, The applications of semiconductor materials in air batteries, Chin. Chem. Lett. 32 (2021) 3277–3287, https://doi.org/10.1016/j.cclet.2021.04.049.

[6] S. Mishra, R. Acharya, Photocatalytic applications of graphene based semiconductor composites: a review, Mater. Today Proc. 35 (2021) 164–169, https://doi.org/10.1016/j.matpr.2020.04.066.

[7] M. Tahir, S. Tasleem, B. Tahir, Recent development in band engineering of binary semiconductor materials for solar driven photocatalytic hydrogen production, Int. J. Hydrogen Energy 45 (2020) 15985–16038, https://doi.org/10.1016/j.ijhydene.2020.04.071.

[8] C. Ros, T. Andreu, J.R. Morante, Photoelectrochemical water splitting: a road from stable metal oxides to protected thin film solar cells, J. Mater. Chem. A 8 (2020) 10625–10669, https://doi.org/10.1039/d0ta02755c.

[9] I. Ahmad, Y. Zou, J. Yan, Y. Liu, S. Shukrullah, M.Y. Naz, H. Hussain, W.Q. Khan, N.R. Khalid, Semiconductor photocatalysts: a critical review highlighting the various strategies to boost the photocatalytic performances for diverse applications, Adv. Colloid Interface Sci. 311 (2023) 102830, https://doi.org/10.1016/j.cis.2022.102830.

[10] Z.H. Jabbar, B.H. Graimed, Recent developments in industrial organic degradation via semiconductor heterojunctions and the parameters affecting the photocatalytic process: a review study, J. Water Process Eng. 47 (2022) 102671, https://doi.org/10.1016/j.jwpe.2022.102671.

[11] P. Calza, M. Minella, L. Demarchis, F. Sordello, C. Minero, Photocatalytic rate dependence on light absorption properties of different TiO2 specimens, Catal. Today 340 (2020) 12–18, https://doi.org/10.1016/j.cattod.2018.10.013.

[12] M.M. Ayyub, C.N.R. Rao, Design of Efficient Photocatalysts through Band Gap Engineering, INC, 2020, https://doi.org/10.1016/B978-0-12-817836-2.00001-6.

[13] H.H. Mohamed, D.W. Bahnemann, The role of electron transfer in photocatalysis: fact and fictions, Appl. Catal. B Environ. 128 (2012) 91–104, https://doi.org/10.1016/j.apcatb.2012.05.045.

[14] R. Sabouni, H. Gomaa, Photocatalytic degradation of pharmaceutical micropollutants using ZnO, Environ. Sci. Pollut. Res. 26 (2019) 5372–5380, https://doi.org/10.1007/s11356-018-4051-2.

[15] W. Gao, Z. Li, Nanostructures of zinc oxide, Int. J. Nanotechnol. 6 (2009) 245–257, https://doi.org/10.1504/IJNT.2009.022917.

[16] D.K. Sharma, S. Shukla, K.K. Sharma, V. Kumar, A review on ZnO: fundamental properties and applications, Mater. Today Proc. 49 (2020) 3028–3035, https://doi.org/10.1016/j.matpr.2020.10.238.

[17] A. Jiang, Y. Yuan, N. Liu, L. Han, M. Xiong, Y. Sheng, Z. Ye, Y. Liu, Transparent capacitive-type fingerprint sensing based on zinc oxide thin-film transistors, IEEE Electron. Device Lett. 40 (2019) 403–406, https://doi.org/10.1109/LED.2019.2895830.

[18] H.K. Liang, S.F. Yu, H.Y. Yang, ZnO random laser diode arrays for stable single-mode operation at high power, Appl. Phys. Lett. 97 (2010), https://doi.org/10.1063/1.3527922.

[19] S.K. Shaikh, V. V Ganbavle, S.I. Inamdar, K.Y. Rajpure, RSC advances, RSC Adv. 6 (2016) 25641–25650, https://doi.org/10.1039/C6RA01750A.

[20] J. Long, M. Fu, C. Li, C. Sun, D. He, Y. Wang, High-quality ZnO inverse opals and related heterostructures as photocatalysts produced by atomic layer deposition, Appl. Surf. Sci. 454 (2018) 112–120, https://doi.org/10.1016/j.apsusc.2018.05.160.

[21] Y. Lin, H. Hu, Y.H. Hu, Role of ZnO morphology in its reduction and photocatalysis, Appl. Surf. Sci. 502 (2020) 144202, https://doi.org/10.1016/j.apsusc.2019.144202.

[22] P. Jongnavakit, P. Amornpitoksuk, S. Suwanboon, T. Ratana, Surface and photocatalytic properties of ZnO thin film prepared by sol-gel method, Thin Solid Films 520 (2012) 5561–5567, https://doi.org/10.1016/j.tsf.2012.04.050.

[25] J. Husna, M. Mannir Aliyu, M. Aminul Islam, P. Chelvanathan, N. Radhwa Hamzah, M. Sharafat Hossain, M.R. Karim, N. Amin, Influence of annealing temperature on the properties of ZnO thin films grown by sputtering, Energy Proc. 25 (2012) 55–61, https://doi.org/10.1016/j.egypro.2012.07.008.

[26] E. Ersöz, O. Altintas Yildirim, Green synthesis and characterization of Ag-doped ZnO nanofibers for photodegradation of MB, RhB and MO dye molecules, J. Korean Ceram. Soc. 59 (2022) 655–670, https://doi.org/10.1007/s43207-022-00202-3.

[27] T.K. Pathak, R.E. Kroon, H.C. Swart, Photocatalytic and biological applications of Ag and Au doped ZnO nanomaterial synthesized by combustion, Vacuum 157 (2018) 508–513, https://doi.org/10.1016/j.vacuum.2018.09.020.

[28] I. Jellal, K. Nouneh, H. Toura, M. Boutamart, S. Briche, J. Naja, B.M. Soucase, M. E. Touhami, Enhanced photocatalytic activity of supported Cu-doped ZnO nanostructures prepared by SILAR method, Opt. Mater. 111 (2021) 110669, https://doi.org/10.1016/j.optmat.2020.110669.

[29] X. Gu, C. Li, S. Yuan, M. Ma, Y. Qiang, J. Zhu, ZnO based heterojunctions and their application in environmental photocatalysis, Nanotechnology 27 (2016) 1–21, https://doi.org/10.1088/0957-4484/27/40/402001.

[30] A. Das, P.M. Kumar, M. Bhagavathiachari, R.G. Nair, Hierarchical ZnO-TiO2 nanoheterojunction: a strategy driven approach to boost the photocatalytic performance through the synergy of improved surface area and interfacial charge transport, Appl. Surf. Sci. 534 (2020) 147321, https://doi.org/10.1016/j.apsusc.2020.147321.
[31] L. Zhipeng, X. X, Y.J. Ligong Zhou, Liying Lu, Enhanced photocatalytic properties of ZnO/Al2O3 nanorod heterostructure, Mater. Res. Express 59 (2013) 145–150, https://doi.org/10.7868/s0023476113060106.
[32] S. Adhikari, D. Sarkar, G. Madras, Highly efficient WO3-ZnO mixed oxides for photocatalysis, RSC Adv. 5 (2015) 11895–11904, https://doi.org/10.1039/c4ra13210f.
[33] A.G. Bekru, L.T. Tufa, O.A. Zelekew, M. Goddati, J. Lee, F.K. Sabir, Green synthesis of a CuO-ZnO nanocomposite for efficient photodegradation of methylene blue and reduction of 4-nitrophenol, ACS Omega 7 (2022) 30908–30919, https://doi.org/10.1021/acsomega.2c02687.
[34] G.I.N. Waterhouse, M.R. Waterland, Opal and inverse opal photonic crystals: fabrication and characterization, Polyhedron 26 (2007) 356–368, https://doi.org/10.1016/j.poly.2006.06.024.
[35] F. Fathi, H. Monirinasab, F. Ranjbary, K. Nejati-Koshki, Inverse opal photonic crystals: recent advances in fabrication methods and biological applications, J. Drug Deliv. Sci. Technol. 72 (2022) 103377, https://doi.org/10.1016/j.jddst.2022.103377.
[36] H. Shen, J. Bai, X. Zhao, B. Lu, D. Han, S. Li, K. Qin, S. Ren, Y. Wang, M. Wang, Y. Lian, Z. Gao, Y. Peng, Highly ordered, plasmonic enhanced inverse opal photonic crystal for ultrasensitive detection of staphylococcal enterotoxin B, ACS Appl. Mater. Interfaces 14 (2022) 4637–4646, https://doi.org/10.1021/acsami.1c18386.
[37] S.R. Kousik, D. Sipp, K. Abitaev, Y. Li, T. Sottmann, K. Koynov, P. Atanasova, From macro to mesoporous zno inverse opals: synthesis, characterization and tracer diffusion properties, Nanomaterials 11 (2021) 1–18, https://doi.org/10.3390/nano11010196.
[38] J. Gao, W. Tian, H. Zhang, S. Wang, Engineered inverse opal structured semiconductors for solar light-driven environmental catalysis, Nanoscale (2022) 14341–14367, https://doi.org/10.1039/d2nr03924a.
[39] A. Ramos-Carrazco, J.A. Gallardo-Cubedo, A. Vera-Marquina, A.L. Leal-Cruz, J. R. Noriega, C. Zuñiga-Islas, A.G. Rojas-Hernández, R. Gomez-Fuentes, D. Berman-Mendoza, Characterization of ZnO films grown by chemical vapor deposition as active layer in pseudo-MOSFET, J. Electron. Mater. 50 (2021) 5196–5208, https://doi.org/10.1007/s11664-021-09038-9.
[40] K.L. Foo, U. Hashim, C.H. Voon, M. Kashif, Fabrication and characterization of ZnO thin films by sol-gel spin coating method for pH measurement, Adv. Mater. Res. 1109 (2015) 99–103. https://doi.org/10.4028/www.scientific.net/amr.1109.99.
[41] D. Karajz, D. Cseh, B. Parditka, Z. Erdélyi, I. Szilágyi, Combining ZnO inverse opal and ZnO nanorods using ALD and hydrothermal growth, J. Therm. Anal. Calorim. (2022), https://doi.org/10.1007/s10973-022-11255-1.
[42] M.R. Alfaro Cruz, O. Ceballos-Sanchez, E. Luévano-Hipólito, L.M. Torres-Martínez, ZnO thin films deposited by RF magnetron sputtering: effects of the annealing and atmosphere conditions on the photocatalytic hydrogen production, Int. J. Hydrogen Energy 43 (2018) 10301–10310, https://doi.org/10.1016/j.ijhydene.2018.04.054.
[43] S.M. George, Atomic layer deposition: an overview, Chem. Rev. 110 (2010) 111–131, https://doi.org/10.1021/cr900056b.
[44] I.M. Szilágyi, G. Teucher, E. Härkönen, E. Färm, T. Hatanpää, T. Nikitin, L. Khriachtchev, M. Räsänen, M. Ritala, M. Leskelä, Programming nanostructured soft biological surfaces by atomic layer deposition, Nanotechnology 24 (2013), https://doi.org/10.1088/0957-4484/24/24/245701.
[45] R.W. Johnson, A. Hultqvist, S.F. Bent, A brief review of atomic layer deposition: from fundamentals to applications, Mater. Today 17 (2014) 236–246, https://doi.org/10.1016/j.mattod.2014.04.026.
[46] C. Detavernier, D. Deduytsche, J. Musschoot, J. Dendooven, Thermal versus plasma-enhanced ALD: growth kinetics and conformality, ECS Meet. Abstr. MA2008-02 (2008), https://doi.org/10.1149/ma2008-02/24/1913, 1913–1913.
[47] R. Lo Nigro, E. Schilirò, G. Mannino, S. Di Franco, F. Roccaforte, Comparison between thermal and plasma enhanced atomic layer deposition processes for the growth of HfO2 dielectric layers, J. Cryst. Growth 539 (2020) 125624, https://doi.org/10.1016/j.jcrysgro.2020.125624.
[48] H.B. Profijt, S.E. Potts, M.C.M. van de Sanden, W.M.M. Kessels, Plasma-assisted atomic layer deposition: basics, opportunities, and challenges, J. Vac. Sci. Technol. A Vacuum, Surfaces, Film. 29 (2011), https://doi.org/10.1116/1.3609974.
[49] L. Aarik, C.T. Piller, J. Raud, R. Talviste, I. Jõgi, J. Aarik, Atomic layer deposition of α-Al2O3 from trimethylaluminum and H2O: effect of process parameters and plasma excitation on structure development, J. Cryst. Growth 609 (2023) 6–11, https://doi.org/10.1016/j.jcrysgro.2023.127148.
[50] C. Guerra-Nuñez, M. Döbeli, J. Michler, I. Utke, Reaction and growth mechanisms in Al2O3 deposited via atomic layer deposition: elucidating the hydrogen source, Chem. Mater. 29 (2017) 8690–8703, https://doi.org/10.1021/acs.chemmater.7b02759.
[51] E. Langereis, M. Bouman, J. Keijmel, M.C. Van de Sanden, W.M. Kessels, Plasma-assisted ALD of Al2O3 at low temperatures: reaction mechanisms and material properties, ECS Meet. Abstr. MA2008-02 (2008), https://doi.org/10.1149/ma2008-02/24/1914, 1914–1914.
[52] S.B.S. Heil, J.L. Van Hemmen, M.C.M. Van De Sanden, W.M.M. Kessels, Reaction mechanisms during plasma-assisted atomic layer deposition of metal oxides: a case study for Al2O3, J. Appl. Phys. 103 (2008), https://doi.org/10.1063/1.2924406.
[53] H.H. Lemago, F.S. Addin, K. Atilla, B. Parditka, D. Hessz, I. Mikl, Synthesis of TiO 2/Al 2 O 3 Double-Layer Inverse Opal by Thermal and Plasma-Assisted Atomic Layer Deposition for Photocatalytic Applications, 2023.
[54] K. Pham, S. Pelisset, N. Kinnunen, P. Karvinen, T.K. Hakala, J.J. Saarinen, Controlled photocatalytic activity of TiO2 inverse opal structures with atomic layer deposited (ALD) metal oxide thin films, Mater. Chem. Phys. 277 (2022) 1–5, https://doi.org/10.1016/j.matchemphys.2021.125533.
[55] M.T. Aguilar-Gama, E. Ramírez-Morales, Z. Montiel-González, A. Mendoza-Galván, M. Sotelo-Lerma, P.K. Nair, H. Hu, Structure and refractive index of thin alumina films grown by atomic layer deposition, J. Mater. Sci. Mater. Electron. 26 (2015) 5546–5552, https://doi.org/10.1007/s10854-014-2111-z.
[56] L. Zhang, H.C. Jiang, C. Liu, J.W. Dong, P. Chow, Annealing of Al2O3 thin films prepared by atomic layer deposition, J. Phys. D Appl. Phys. 40 (2007) 3707–3713, https://doi.org/10.1088/0022-3727/40/12/025.
[57] A.R. Zanatta, Revisiting the optical bandgap of semiconductors and the proposal of a unified methodology to its determination, Sci. Rep. 9 (2019) 11225, https://doi.org/10.1038/s41598-019-47670-y.
[58] M. Chitra, G. Mangamma, K. Uthayarani, N. Neelakandeswari, E.K. Girija, Band gap engineering in ZnO based nanocomposites, Phys. E Low-Dimensional Syst. Nanostructures. 119 (2020) 113969, https://doi.org/10.1016/j.physe.2020.113969.
[59] A.F. Alamouti, M. Nadafan, Z. Dehghani, M.H.M. Ara, A.V. Noghreiyan, Structural and optical coefficients investigation of γ-Al2O3 nanoparticles using kramers-kronig relations and Z–scan technique, J. Asian Ceram. Soc. 9 (2021) 366–373, https://doi.org/10.1080/21870764.2020.1869881.
[60] T. Baba, Slow light in photonic crystals, Nat. Photonics 2 (2008) 465–473, https://doi.org/10.1038/nphoton.2008.146.
[61] T. Raja-Mogan, B. Ohtani, E. Kowalska, Photonic crystals for plasmonic photocatalysis, Catalysts 10 (2020) 1–20, https://doi.org/10.3390/catal10080827.
[62] J.B. Coulter, D.P. Birnie, Assessing tauc plot slope quantification: ZnO thin films as a model system, Phys. Status Solidi Basic Res. 255 (2018) 1–7, https://doi.org/10.1002/pssb.201700393.
[63] K. Tanaka, Minimal Urbach energy in non-crystalline materials, J. Non-Cryst. Solids 389 (2014) 35–37, https://doi.org/10.1016/j.jnoncrysol.2014.02.004.
[64] A. Boukhachem, B. Ouni, M. Karyaoui, A. Madani, R. Chtourou, M. Amlouk, Structural, opto-thermal and electrical properties of ZnO:Mo sprayed thin films, Mater. Sci. Semicond. Process. 15 (2012) 282–292, https://doi.org/10.1016/j.mssp.2012.02.014.
[65] C. Zhang, Q. Tu, L.F. Francis, U.R. Kortshagen, Band gap tuning of films of undoped ZnO nanocrystals by removal of surface groups, Nanomaterials 12 (2022), https://doi.org/10.3390/nano12030565.
[66] J. López, E. Solorio, H.A. Borbón-Nuñez, F.F. Castillón, R. Machorro, N. Nedev, M. H. Farías, H. Tiznado, Refractive index and bandgap variation in Al2O3-ZnO ultrathin multilayers prepared by atomic layer deposition, J. Alloys Compd. 691 (2017) 308–315, https://doi.org/10.1016/j.jallcom.2016.08.271.
[67] H. Noh, M. Scharrer, M.A. Anderson, R.P.H. Chang, H. Cao, Photoluminescence modification by a high-order photonic band with abnormal dispersion in ZnO inverse opal, Phys. Rev. B Condens. Matter 77 (2008) 1–9, https://doi.org/10.1103/PhysRevB.77.115136.
[68] M. Scharrer, X. Wu, A. Yamilov, H. Cao, R.P.H. Chang, Fabrication of inverted opal ZnO photonic crystals by atomic layer deposition, Appl. Phys. Lett. 86 (2005) 1–3, https://doi.org/10.1063/1.1900957.
[69] J. Lv, C. Li, Z. Chai, Defect luminescence and its mediated physical properties in ZnO, J. Lumin. 208 (2019) 225–237, https://doi.org/10.1016/j.jlumin.2018.12.050.
[70] C. Yang, Q. Li, ZnO inverse opals with deposited Ag nanoparticles: fabrication, characterization and photocatalytic activity under visible light irradiation, J. Photochem. Photobiol. Chem. 371 (2019) 118–127, https://doi.org/10.1016/j.jphotochem.2018.10.039.
[71] J. Liu, J. Jin, Y. Li, H.W. Huang, C. Wang, M. Wu, L.H. Chen, B.L. Su, Tracing the slow photon effect in a ZnO inverse opal film for photocatalytic activity enhancement, J. Mater. Chem. A 2 (2014) 5051–5059, https://doi.org/10.1039/c3ta15044e.
[72] C. Yang, W. Dong, G. Cui, Y. Zhao, X. Shi, X. Xia, B. Tang, W. Wang, Highly efficient photocatalytic degradation of methylene blue by P2ABSA-modified TiO2 nanocomposite due to the photosensitization synergetic effect of TiO2 and P2ABSA, RSC Adv. 7 (2017) 23699–23708, https://doi.org/10.1039/c7ra02423a.
[73] A.V. Mohod, M. Momotko, N.S. Shah, M. Marchel, M. Imran, L. Kong, G. Boczkaj, Degradation of rhodamine dyes by advanced oxidation processes (AOPs) – focus on cavitation and photocatalysis - a critical review, Water Resour. Ind. 30 (2023), https://doi.org/10.1016/j.wri.2023.100220.
[74] N. Yudasari, R. Anugrahwidya, D. Tahir, M.M. Suliyanti, Y. Herbani, C. Imawan, M. Khalil, D. Djuhana, Enhanced photocatalytic degradation of rhodamine 6G (R6G) using ZnO–Ag nanoparticles synthesized by pulsed laser ablation in liquid (PLAL), J. Alloys Compd. 886 (2021) 161291, https://doi.org/10.1016/j.jallcom.2021.161291.
[75] S.S. Shenouda, M.S.A. Hussien, B. Parditka, A. Csík, V. Takats, Z. Erdélyi, Novel amorphous Al-rich Al2O3 ultra-thin films as active photocatalysts for water treatment from some textile dyes, Ceram. Int. 46 (2020) 7922–7929, https://doi.org/10.1016/j.ceramint.2019.12.012.
[76] B. Hu, M. Yao, R. Xiao, J. Chen, X. Yao, Optical properties of amorphous Al2O3 thin films prepared by a sol-gel process, Ceram. Int. 40 (2014) 14133–14139, https://doi.org/10.1016/j.ceramint.2014.05.148.
[77] J. Gao, X. Sun, Y. Wang, Y. Li, X. Li, C. Chen, J. Ni, Ultrathin Al2O3 passivation layer-wrapped Ag@TiO2 nanorods by atomic layer deposition for enhanced

photoelectrochemical performance, Appl. Surf. Sci. 499 (2020), https://doi.org/10.1016/j.apsusc.2019.143971.

[78] M. Nasr, R. Viter, C. Eid, R. Habchi, P. Miele, M. Bechelany, Optical and structural properties of Al2O3 doped ZnO nanotubes prepared by ALD and their photocatalytic application, Surf. Coating. Technol. 343 (2018) 24–29, https://doi.org/10.1016/j.surfcoat.2017.11.060.

[79] J.H. Jeong, J.S. Shin, J.H. Ma, S.J. Kang, S.J. Kang, Highly enhanced visible light photodetection properties of a ZnO phototransistor via an additional solution processed thin Al2O3 layer, J. Mater. Chem. C 10 (2022) 14770–14777, https://doi.org/10.1039/d2tc02500k.